

Monitoring Fires with the GOES-R Series

Chris Schmidt

Cooperative Institute for Meteorological Satellite Studies (CIMSS), University of Wisconsin-Madison, Madison, WI,
United States

13.1 MONITORING FIRES FROM GEOSTATIONARY ORBIT

On days when the air and vegetation are dry and the winds are expected to be high, National Weather Service (NWS) forecasters in Norman, Oklahoma, watch Advanced Baseline Imager (ABI) imagery very closely, looking for tell-tale heat signatures of fires in animations of Geostationary Operational Environmental Satellite (GOES)-16 Level 1b (L1b) imagery. The 1-min cadence of the mesoscale sector offers the opportunity for speedy identification of potential hotspots at their earliest stages, and once a suspicious hotspot is identified, an alert is sent out. While there are occasional false alarms, and some hotspots are due to gas flares at petroleum operations or other man-made sources, emergency managers on the ground are willing to accept those for the benefit of catching other incidents early. They have seen the devastation, and death, that can result from grassland fires in Oklahoma, Texas, and Kansas, fires that advance faster than had been thought possible, hopping over earthworks and fire lines as the winds carry embers forward (Hollandsworth, 2017).

The improved resolution in space and time provided by ABI is leading to a major change in how fire detection from geostationary satellites is perceived and utilized. However, geostationary fire detection, both manual and automated, did not start with ABI. It dates back at least to the days of the GOES-7 Visible Infrared Spin Scan Radiometer (VISSR) Atmospheric Sounder (VAS), a 10-km sounder that had IR window bands, like the 11.2- and 3.9- μm bands, the latter of which is good for seeing fires. Fires could be manually picked out either directly in the 3.9- μm band or in a band difference with the 11.2- μm band. It was with that data that Elaine Prins of the Cooperative Institute for Meteorological Satellite Studies (CIMSS) at the Space Science Engineering Center (SSEC) at the University of Wisconsin-Madison began development in the 1990s of the automated biomass burning algorithm (ABBA). Aside from detecting fires, ABBA implemented the “Dozier Technique,” described by Matson and Dozier in 1981, to calculate estimates of the instantaneous fire size and temperature (Matson and Dozier, 1981; Prins and Menzel, 1992, 1994; Prins and Schmidt, 2001).

Beginning in 1994, the GOES-8 through -15 imagers provided substantially better fire detection and characterization capability. With 4-km resolution and higher temporal refresh rate, including three hourly full-disk (FD) images and 15-min images over the contiguous US (CONUS), automation of fire detection became a necessity if one sought to get the most out of the data. At the time the slash and burn practices in the Amazon Basin drove interest in development of the algorithm. ABBA made use of the 3.9- and 11.2- μm bands on GOES-8, as well as the uncalibrated visible (0.64 μm) band, to locate and attempt to characterize the fires. Rather than relying just on static thresholds, it was a contextual algorithm that had to contend with a complex background: rainforest with treeless gaps that look warm in the infrared (IR) band, daily incursions of small clouds that reflected sunlight, solar reflections off bodies of water, and other complications. Aside from researchers in South America who were working to track the slash and burn agriculture that was tearing through the Amazon Basin, the primary users in those waning days of the 20th century were aerosol and smoke modelers. NWS and US Forest Service (USFS) did not see the geostationary platform as a source for fire information—early detection over CONUS with a sufficiently low false alarm rate had not yet been demonstrated with the ABBA.

Things changed in 2000 when Donna McNamara, the Environmental Applications Team Leader at the National Oceanic and Atmospheric Administration's (NOAA's) National Environmental Satellite, Data, and Information Service (NESDIS) Office of Satellite Data Processing and Distribution (OSDPD) Satellite Services Division Interactive Processing Branch, and Elaine Prins put together a plan for transitioning the wildfire ABBA (WFABBA), as the hemisphere-wide ABBA was christened, from research to operations. That pathway, with the CIMSS team providing the operational system, was an experiment. And it worked. By late 2002, WFABBA was an operational product, primarily seeing use as an input for the NOAA Hazard Mapping System, which combined satellite fire products, imagery, and the judgment of human operators to produce quality-controlled fire location and smoke extent products. Requests from aerosol modelers working for the US Navy to run WFABBA on data from the European Organisation for the Exploitation of Meteorological Satellites (EUMETSAT's) Meteosat Second Generation (MSG) series and Japan's Multi-functional Transport Satellite (MTSAT) series led to support of those satellites as well. Despite some critical differences, all of the platforms shared similar radiometric bands, and the algorithm itself was not strictly wed to the GOES imager architecture (McNamara et al., 2002).

Thanks to its legacy as an operational product, the fire detection and characterization algorithm (FDCA), sometimes known as "fire/hot spot" (FHS), was designated a baseline product for the GOES-R Series. FDCA is WFABBA adapted for ABI, which allowed the algorithm to take advantage of the improved radiometric performance and resolution of ABI, though the full advantages of the temporal resolution of ABI data was not integrated into the algorithm. Fire detection guided the specifications for the 3.9- μm band (band 7), specifically the saturation temperature of at least 400 K. Saturation is the point where a sensor cannot read a higher signal. While most older GOES had 3.9- μm saturation temperatures around 335–340 K, some GOES imagers and other instruments saturated as low as 320 K or less, which often led to saturation over large areas of ground and of a large fraction of detected fires without properties due to saturation. The 400 K threshold was chosen to keep the fraction of detected fires that were associated with saturated pixels below 2%, the fraction observed with GOES-8 and -12.

13.2 PHYSICS OF FIRE DETECTION

When considering geostationary weather observation, we usually think in terms of two different regimes: long-wave IR emitted by Earth and its atmosphere, and the shortwave IR and visible reflected sunlight. For the most part under normal conditions, those two regimes are independent of each other, except around 4 μm where the two intersect. Bands around 4 μm exhibit both emission and reflection from Earth's surface, making them useful for cloud products and in other cases. Four micrometers also happens to be in the range of wavelengths where terrestrial heat sources like fires have their peak emission. Fig. 13.1 illustrates the Planck curves for heat sources of various temperatures. Earth and clouds emit in roughly the 200–300 K range, with peak emission spread throughout the longwave IR. Fires have a broader range, from about 400 to 2000 K, with peak emission in the 3–4- μm range. The Sun emits at 5778 K, its peak emissive wavelength about 500 nm. Also plotted over those curves are the band coverage of the 16 ABI bands.

As Fig. 13.1 shows, fires do not just emit radiation near 4 μm . They can be seen in most ABI bands if they are sufficiently hot and/or occupy a large enough fraction of the pixel. Fig. 13.2 illustrates this using the Tubbs Fire on October 9, 2017, which occurred north of San Francisco Bay. The Tubbs Fire started overnight and was stoked by Santa Ana winds, and it and neighboring fires exploded very rapidly. All 16 bands are shown in Fig. 13.2, each enhanced to bring out the fire signal if present in that band. In general, if a hotspot can be seen in the "blue" and "red" visible bands, that suggests an event of nuclear origin. Otherwise, some fire signal can be teased out of most bands except some water vapor bands where the intervening vapor absorbs the signal. O_3 absorption in band 12 and CO_2 absorption in band 16 also notably diminish the fire signal (as they do with the rest of the surface emissions). While fires show up pretty well in bands 5 and 6, they are less sensitive than band 7. More importantly, bands 5 and 6 are dominated by solar reflection during the day, making fire detection with those bands difficult. Fig. 13.3 shows the Tubbs Fire at the same location around local noon in all 16 bands (Animation 13.1 in the online version at <https://doi.org/10.1016/B978-0-12-814327-8.00013-5>). While the fire signal can be seen in bands 5 and 6, it is less obvious and harder to separate from the background than it was at night.

Fires, unlike most phenomena observed by GOES-16, are subpixel entities. Their radiometric signature depends on their temperature and their size. Most of the time they occupy a small fraction of the pixel's nominal, square field of view, but are discernable because they produce 10–100 times more radiation than the surrounding area. This stark contrast also makes them sensitive to diffraction, an unavoidable reality that causes the spatial response of a pixel to vary across its field of view. The center of a pixel contributes more energy to the total than the edges, with the

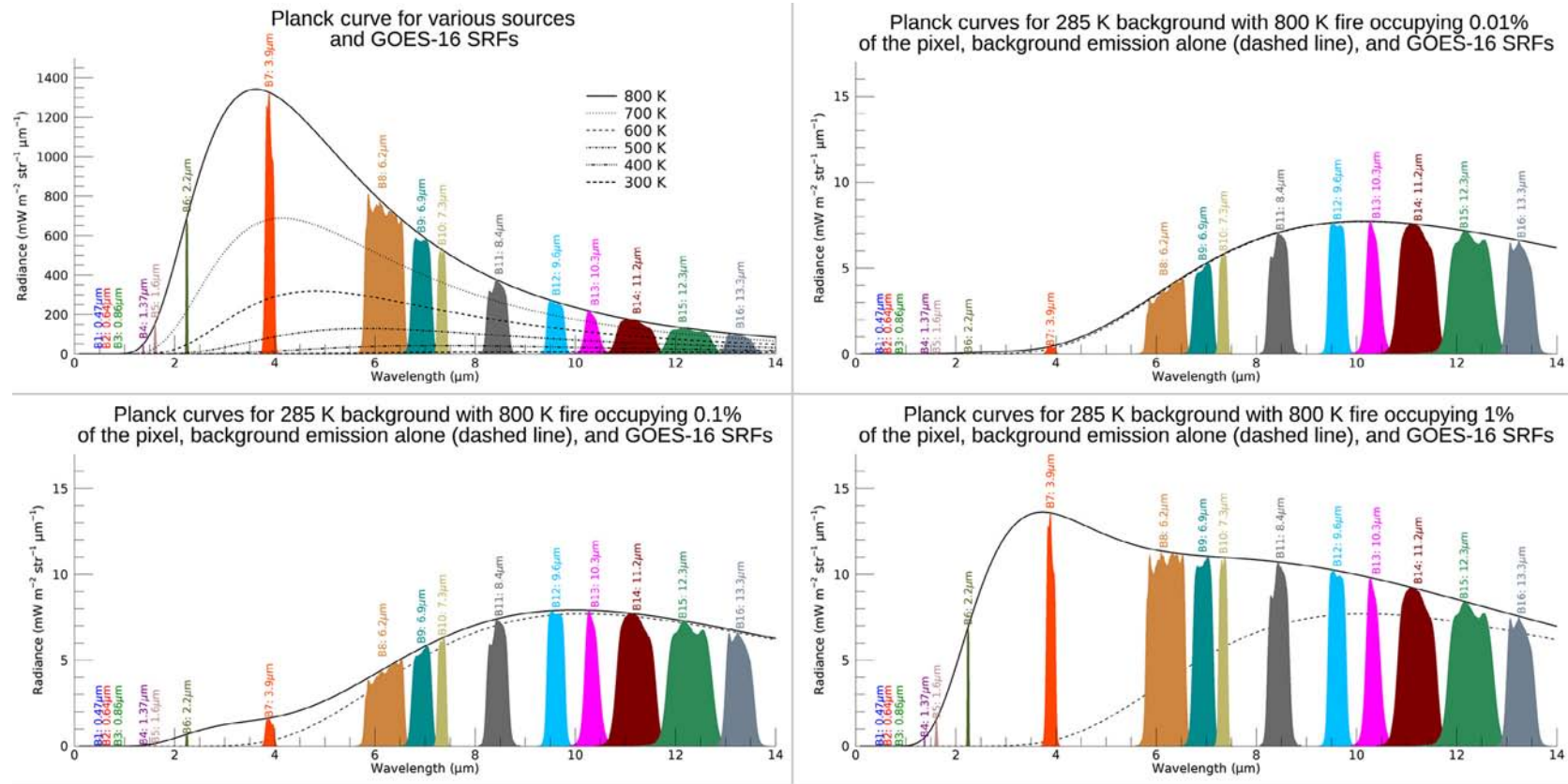


FIG. 13.1 Planck curves with ABI spectral response functions for various scenarios. The upper left panel illustrates Planck curves for various emitting source temperatures. The remaining panels (cont'd on next page) illustrate how different heat sources that are similar to various fire scenarios affect the emissions. The lower right panel (next page) represents modest solar reflection, which primarily impacts the shortwave bands and provides some contribution around 4 μm .

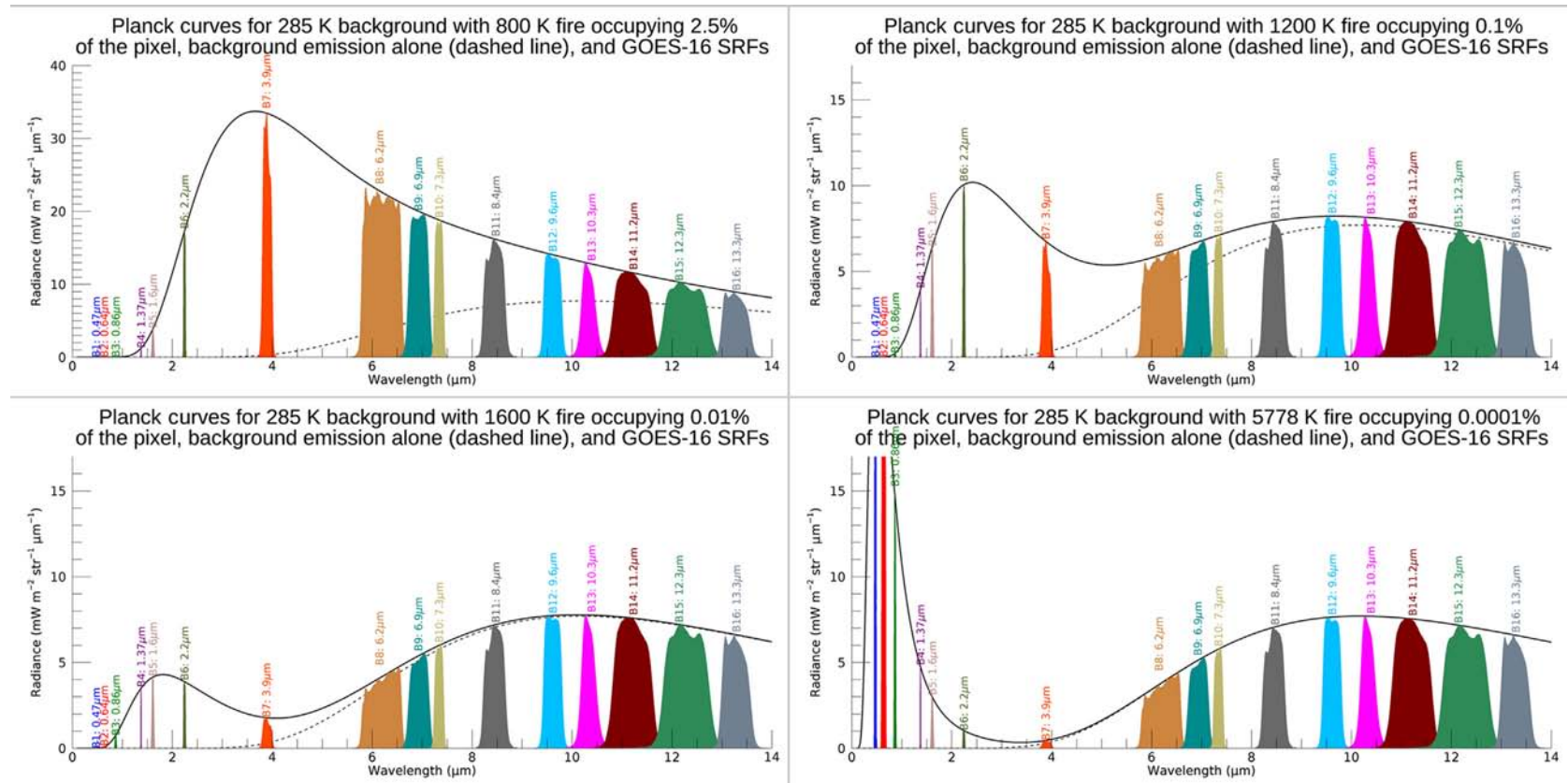


FIG. 13.1, CONT'D

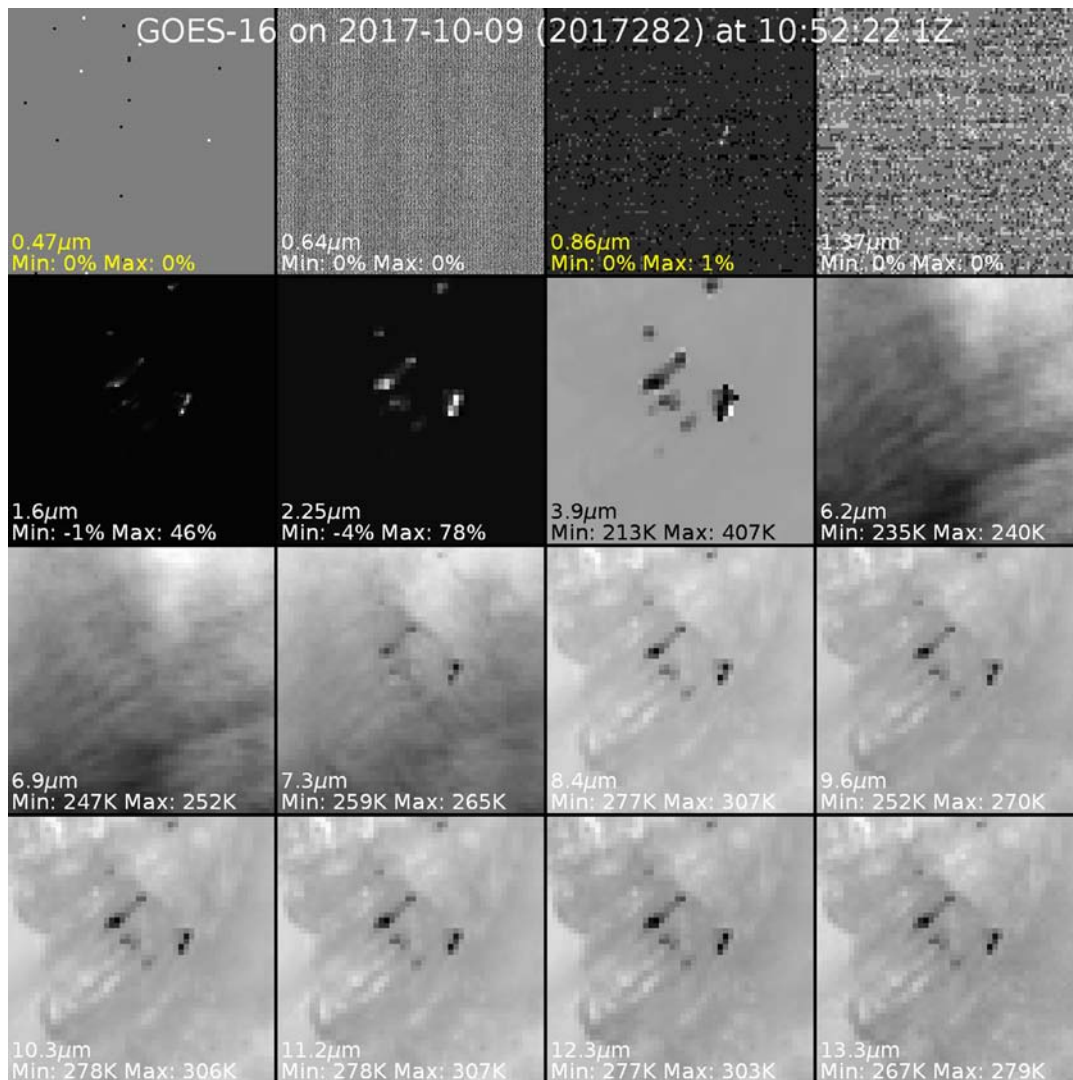


FIG. 13.2 The Tubbs Fire as observed by all 16 ABI bands at night. The bands have been scaled to the data in the scene to maximize contrast, with the respective minimum and maximum noted for each. For shortwave bands at $2.2\mu\text{m}$ and below, the most reflective pixels in the scene are white and the least reflective are black. For longwave IR bands at and above $3.9\mu\text{m}$, white is the coldest and black is the hottest pixel in the scene. The visible bands are dominated by noise, as is $1.37\text{-}\mu\text{m}$ band, which rarely shows emission from the surface. During the daytime, the 1.6- and $2.2\text{-}\mu\text{m}$ bands would be dominated by surface reflection, but at night they will pick up fire emissions for hotter fires (as seen in Fig. 13.1). The $3.9\text{-}\mu\text{m}$ band is the most sensitive to fire. The 6.2- and $6.9\text{-}\mu\text{m}$ bands show no fire signal due to water vapor absorption, but the remaining longwave IR bands show fire signal to varying degrees depending on the amount of water vapor, ozone, and carbon dioxide absorption at those wavelengths.

spatial response following a roughly Gaussian shape. For this same reason, some contribution to the sample total comes from outside of the footprint. ABI and other imagers are designed to control this and minimize its impact, and most other phenomena observed by GOES are not subpixel in character coupled with very high radiances as fires are. When the signal for a part of the field of view is emitting radiance at one or two orders of magnitude more than the rest of the field of view, the resulting observation can be highly distorted due to this uneven spatial response. If the fire lands in the center of the sample, its apparent output could appear to be two or three, or more, times greater than it is. Conversely, it will appear muted at the edge of the field of view, and “bleed” into the neighboring pixels because their spatial response extends beyond the field of view. The spatial response places a fundamental limit on the accuracy of any single characterization of a fire, particularly for small and hot fires.

Aside from instrument effects, other factors can complicate the detectability of fires. Fires must of course be hot and/or large enough to produce a discernable energy signature. The minimum threshold for human visual detection of fires in ABI imagery is pretty low; a house fire, small controlled burn under an acre, or a gas flare can be seen raising L1b brightness temperatures by even just a fraction of a Kelvin. The algorithm’s threshold is higher, requiring an increase of at least 2K, roughly equivalent to a typical small, controlled burn of about an acre/0.4 ha or so in area

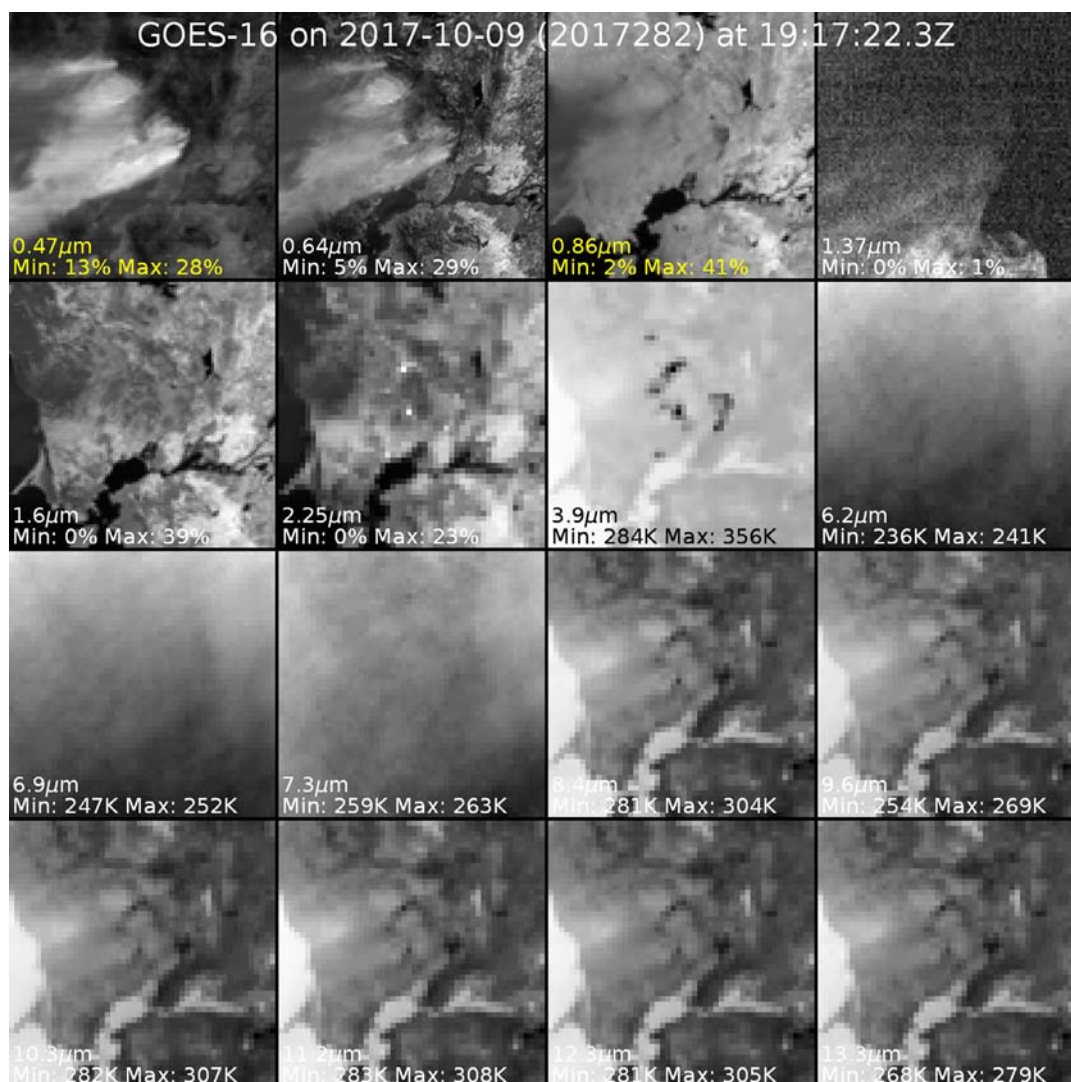


FIG. 13.3 Images of the Tubbs Fire from all 16 ABI bands at approximate local noon. The fire was less intense, producing a lower maximum temperature in the 3.9- μm band. The lower intensity and solar reflections prevent the fire from being visible in the 0.86- and 1.6- μm bands, and only the hottest component can be found in the 2.2- μm band, though without other information that point may not appear to be a fire to most observers. In the longwave bands above 3.9 μm the fire is harder to see, being fairly similar to other nearby non-fire features in the image. Animation 13.1 of this figure is available in the online version at <https://doi.org/10.1016/B978-0-12-814327-8.00013-5>.

under good observing conditions. Cloud cover is the primary cause of missed fires, though fires shine through cirrus clouds and optically thin water clouds, as well as through most smoke from burning biomass. Smoke that originates from some sources, such as oil or tire fires, is relatively opaque and can obscure the source fire. Terrain is also a factor; a fire on a mountain face that a satellite cannot see will not be as well detected, if at all. In urban areas, buildings, or parts of them, can perform similar screening of the fire signal. This was observed in Sun Prairie, Wisconsin, on July 10, 2018 after a gas main explosion in the center of downtown set multiple structures ablaze. The walls on the south side of the buildings were largely left standing, blocking the view of GOES-16, which did not register a strong heat signature from the large blaze.

Manipulation of ABI L1b satellite data can also alter the appearance of fires. ABI data, as well as data from the MSG imagers that preceded ABI, and every new geostationary and polar instrument capable of fire detection, are remapped, taking the calibrated, observed data samples (detector measurements) and projecting them onto a perfect grid of pixels. This has some big advantages for many applications, and for most physical features and applications the remapping has no noticeable impact. However, hotspots radiate substantially above their background, and because remapping kernels look at neighboring instrument samples (in the case of ABI, a 4 \times 4 grid of weighted values), the signal “bleeds” much the same way as it does with diffraction, but to a greater degree. On ABI, this

leads to almost all small hotspots producing a 2×2 pixel signature, though it may not be easy to see without strong enhancement to bring out the detail. Large fires tend to appear a bit larger than they are around the edges due to this process. The initial remapping kernel was a truncated sinc function, and the corners had small negative coefficients. Those “tails” produced extremely cold pixels as much as two pixels away from very hot pixels on the edges of larger fire events. These are known as “cold pixels around fire” (CPAF). Figs. 13.2 and 13.3 show examples of the 2×2 pixel shape and CPAF was visible in the band $3.9\text{-}\mu\text{m}$ panel of Figs. 13.2 and 13.3. Examples of both will be visible in many of the following figures that contain $3.9\text{-}\mu\text{m}$ data. Updates to the resampling kernel effectively eliminated CPAF from ABI data as of April 23, 2019.

13.3 THE ALGORITHM

FDCA produces four outputs: a metadata mask and, for a subset of the detected fires, fire size, fire temperature, and fire radiative power (FRP). The metadata mask includes information on every pixel. For fire pixels, it includes a code indicating which of the six categories was assigned. For other pixels, the mask tells users whether the pixel was considered fire-free land, covered by opaque cloud, or excluded because of solar reflections, bad data, or unusable surface types like water and bare rock.

The six fire categories grew from the requests and requirements of the earliest users of ABBA. The highest confidence category, “processed,” comes with associated instantaneous fire size, temperature, and radiative power. “Saturated” fires are high confidence fire pixels but due to saturation, no properties are calculated. “Cloud-covered” fires are likely fire pixels that appear to have cloud cover due to either longwave IR temperature or high visible albedo, and no properties are provided for fires in this category. “High possibility,” “medium possibility,” and “low possibility” fires do not meet the stricter criteria for “processed” fires. “High” and “medium possibility” fires do have FRP, but it is not provided for “low possibility” fires. Most false positives are “low possibility” fires, a category designed for users with a high tolerance for false alarms.

Locating fires reliably requires distinguishing them from the background scene. To do this, most algorithms rely on comparing the $\sim 4\text{-}\mu\text{m}$ and $\sim 11\text{-}\mu\text{m}$ bands (ABI bands 7 and 14) under the presumption that the differences between the two are primarily due to emissions from fire and, if during the day, reflected sunlight. Surface emissivity also contributes to the variation. Contextual algorithms go beyond just looking at the absolute difference between the observed $4\text{-}\mu\text{m}$ band and what the $11\text{-}\mu\text{m}$ band suggests the $4\text{-}\mu\text{m}$ band would be without fire; they also consider the pixels within a nearby window to better estimate what the background without fire should be. This is necessary because the $11\text{-}\mu\text{m}$ also exhibits a fire signature in some cases. Doing so requires examining the neighborhood of each potential fire pixel and skipping over cloudy pixels and those that are likely also fires. Criteria for both are set specifically for this background calculation. Once a background value is estimated, further processing of the detected fire can commence. In the FDCA, two methods are used to estimate background temperature. One utilizes statistics and searches for a background temperature with a small standard deviation. The other uses a histogram-based approach to find the most common temperature in the background window. The two methods complement each other and incrementally increase the number of potential fire pixels with a valid background temperature until at least 20% of the pixels in the window are considered valid for use in estimating the background temperature.

Once the potential fire is identified, its radiance signature is corrected for water vapor absorption using a lookup table (LUT). The absorption factors are not large and they vary with a zenith angle (and thus depth of atmosphere). The table is divided up into a small number of bins. Both the fire and background signals are corrected. A small diffraction correction is also added. The corrected $4\text{-}\mu\text{m}$ and $11\text{-}\mu\text{m}$ brightness temperatures are then used when calculating fire characteristics.

While size and temperature seem to be self-explanatory, there is a critical caveat: as the results of the Dozier method mentioned earlier, size and temperature represent a hypothetical fire that would produce the same *observed* radiance signal for that pixel. That means they are not necessarily representative of the actual burning area, and fires have a range of temperatures from hot as blazes, so to speak, to smoldering. Size and temperature together can be used to estimate the emissions from the fire, but in terms of the burning area and its temperature they provide a vague qualitative sense at best. Eqs. (13.1) and (13.2) are the two simultaneous equations solved in the Dozier method. In order to fully account for observed energy, a term is added to the $4\text{-}\mu\text{m}$ equation to account for reflected solar radiation.

$$L_4(T_4) = pL_4(T_t) + (1-p)L_4(T_b) + (1-\varepsilon_4)\tau_{4s}L_{4solar} \quad (13.1)$$

$$L_{11}(T_{11}) = pL_{11}(T_t) + (1-p)L_{11}(T_b) \quad (13.2)$$

L_4 and L_{11} are the 4- and 11- μm radiances at the given temperatures. T_4 and T_{11} are the observed 4- and 11- μm brightness temperatures. T_b is the estimated background temperature. ε_4 is the 4- μm emissivity of the surface and τ_{4s} is the transmittance of 4- μm radiance through the atmosphere. $L_{4\text{solar}}$ is the reflected solar radiance at 4 μm . These simultaneous equations are solved for p , the fraction of the pixel on fire, and T_f , the fire temperature (Prins and Menzel, 1992).

FRP is a relatively recent addition to the algorithm outputs. As the time derivative of the fire radiative energy (FRE), FRP gives a direct pathway to calculate the total energy output of a fire by integrating FRP over time. FRE is related to the mass consumed by the heat of combustion, which is pretty similar for most biomass. The fundamental definition of power is in terms of size and area, per Eq. (13.3):

$$\text{Power} = A\varepsilon\sigma T^4 \quad (13.3)$$

A is the area of the emitting body, ε is the emissivity, σ is the Stephan-Boltzman Constant, and T is the blackbody temperature. For a pixel containing n number of burning components, FRP can be expressed as

$$\text{FRP} = A_{\text{pixel}}\varepsilon\sigma \sum_{k=1}^n p_k T_k^4 \quad (13.4)$$

A_{pixel} is the area of the pixel, ε is the emissivity, σ is the Stephan-Boltzman Constant, and the burning components occupying pixel fraction p_k burning at T_k are added together.

Rather than use outputs of the Dozier method as p and T , FDCA and other algorithms exploit the roughly linear relationship between FRP and temperature to the fourth power in the biomass burning temperature regime to calculate FRP from the difference in fire and background radiances in the ABI 3.9- μm band, shown in Eq. (13.5). This approach saves computational time and is less sensitive to error.

$$\text{FRP} = \frac{A_{\text{pixel}}}{d} (L_4 - L_{4b}) \quad (13.5)$$

A_{pixel} is the area of the pixel, L_4 is the observed mid-IR (in this case 3.9 μm) radiance, L_{4b} is the estimated mid-IR (3.9 μm) background radiance, and d is a constant based on the instrument's spectral response function. The approximation is valid for a range of wavelengths where radiance and T^4 are roughly linearly related (Wooster et al., 2003).

It is quite common to find different fire categories in the same complex, be they saturated pixels at the center of a large fire surrounded by processed pixels, cloud covered fire pixels under the smoke plume, or lower possibility fires on the edges of the complex.

13.4 USING ABI L1B IMAGERY AND L2 FIRE DETECTION AND CHARACTERIZATION DATA FOR FIRE MONITORING

On any given day, during virtually any ABI scan of large geographic extent, one can likely find at least one FDCA detected fire, and if not they can be found by visual inspection of the 3.9- μm band 7 imagery. Hot spots in the imagery can be due to wildfires, agricultural burning, controlled burns for wildland management, flares from petroleum operations, structure fires, power plant cooling ponds surrounded by cool cropland, urban areas, and even reflections off solar power facilities.

Structure fires were hardly on the minds of ABI's designers, but it was a structure fire that became the subject of the first ABI Level 2 product to be pushed out on social media by a NWS office. In the early morning hours of July 7, 2017, an apartment building under construction near downtown Oakland was set ablaze by an arsonist. The Bay Area NWS office later that day shared an Advanced Weather Interactive Processing System (AWIPS) screenshot of the fire characteristics for the apartment building fire to illustrate the new FDCA data they were learning to make use of (Fig. 13.4).

The fire was contained to less than a city block and the view of it was partially blocked by the structure, but it was still observed by GOES-16, then at 89.5°W, as shown in Fig. 13.5, which shows a time sequence of bands 7 and 14 and the fire metadata mask from the FDCA. The lack of sunlight makes this an easy case to study; the background is pretty uniform and lacks complicating factors such as clouds. The heat signature is visible to the human eye before the algorithm detects it (Animation 13.2 in the online version at <https://doi.org/10.1016/B978-0-12-814327-8.00013-5>). That is due to the minimum detection thresholds built into the algorithm. In the absence of sunlight, the band 7 brightness temperature has to be at least 2–4 K higher than the band 14 temperature before it is considered a possible fire.

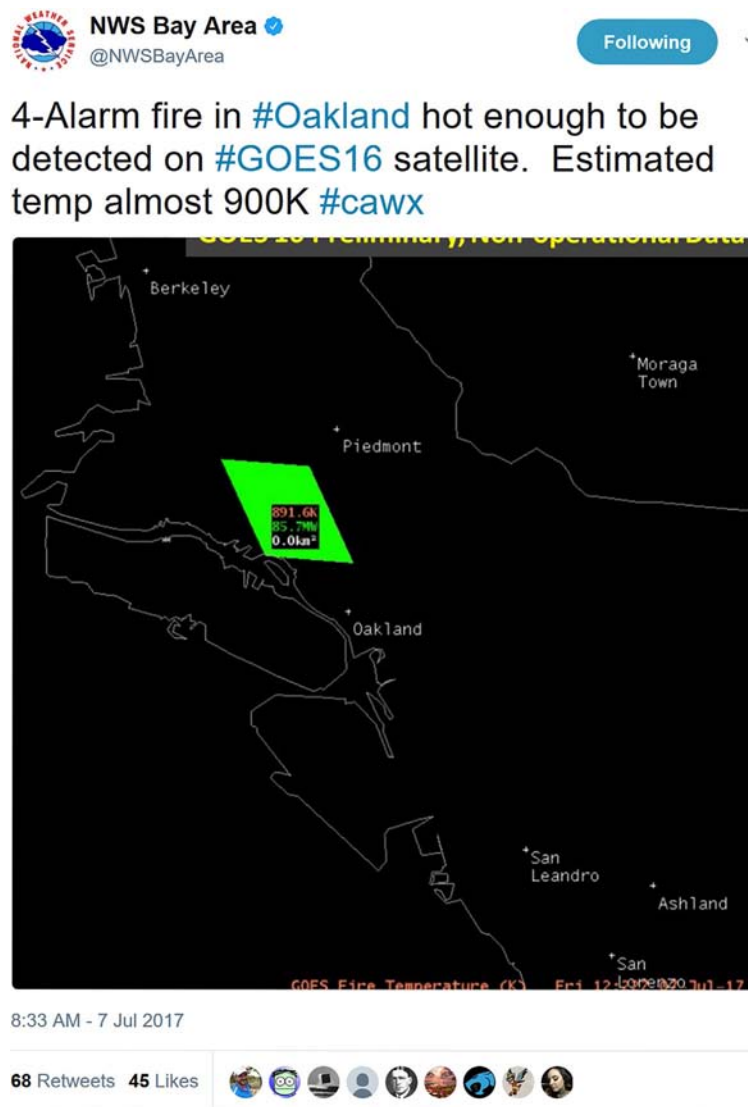


FIG. 13.4 Tweet from @NWSBayArea showing the AWIPS display of the fire products for an apartment complex fire in Oakland, CA. The complex was under construction and the fire was deemed to be arson.

The Oakland apartment building arson case roughly illustrates the lower limits of the FDCA's abilities.

The calibrated L1b data can be very revealing to the human eye, and is useful in cases where early detection is of prime importance. As described earlier, during the spring, on days with high fire risk, the Norman, Oklahoma, NWS office dedicates time to monitoring band 7 (3.9 μm) imagery. One of ABI's mesoscale sectors is often placed over the Plains on those high-risk days, and forecasters watch for fire signals. When they see something suspicious, they report it to local emergency management services. The goal is to stop small fires before they become very large. NWS forecasters have learned how to exploit the remapping artifacts to improve the location of the hotspot to within less than half a pixel, visually identifying the centroid of the 2×2 pixel heat signature. They get feedback from people who check out their hotspots, and at times have learned that their detected fire was not a wildfire but rather a gas flare from a fracking operation or a structure fire. Fig. 13.6 shows band 7 imagery for one such structure fire case from March 6, 2018, where a small signature, about 1 K above the background, proved to be a house fire (Lindley et al., 2016) (Animation 13.3 in the online version at <https://doi.org/10.1016/B978-0-12-814327-8.00013-5>).

NWS's vigilance in Oklahoma is due to the devastation wrought by grassland fires that have been increasing in frequency over the last 10–20 years. One such major event occurred on March 6, 2017, when a mid-latitude cyclone brought 50-mph winds to the drought-stricken Plains. Multiple fires erupted in the Texas Panhandle and raced northeast, killing people and livestock and destroying property. The winds eventually shifted and the fires began

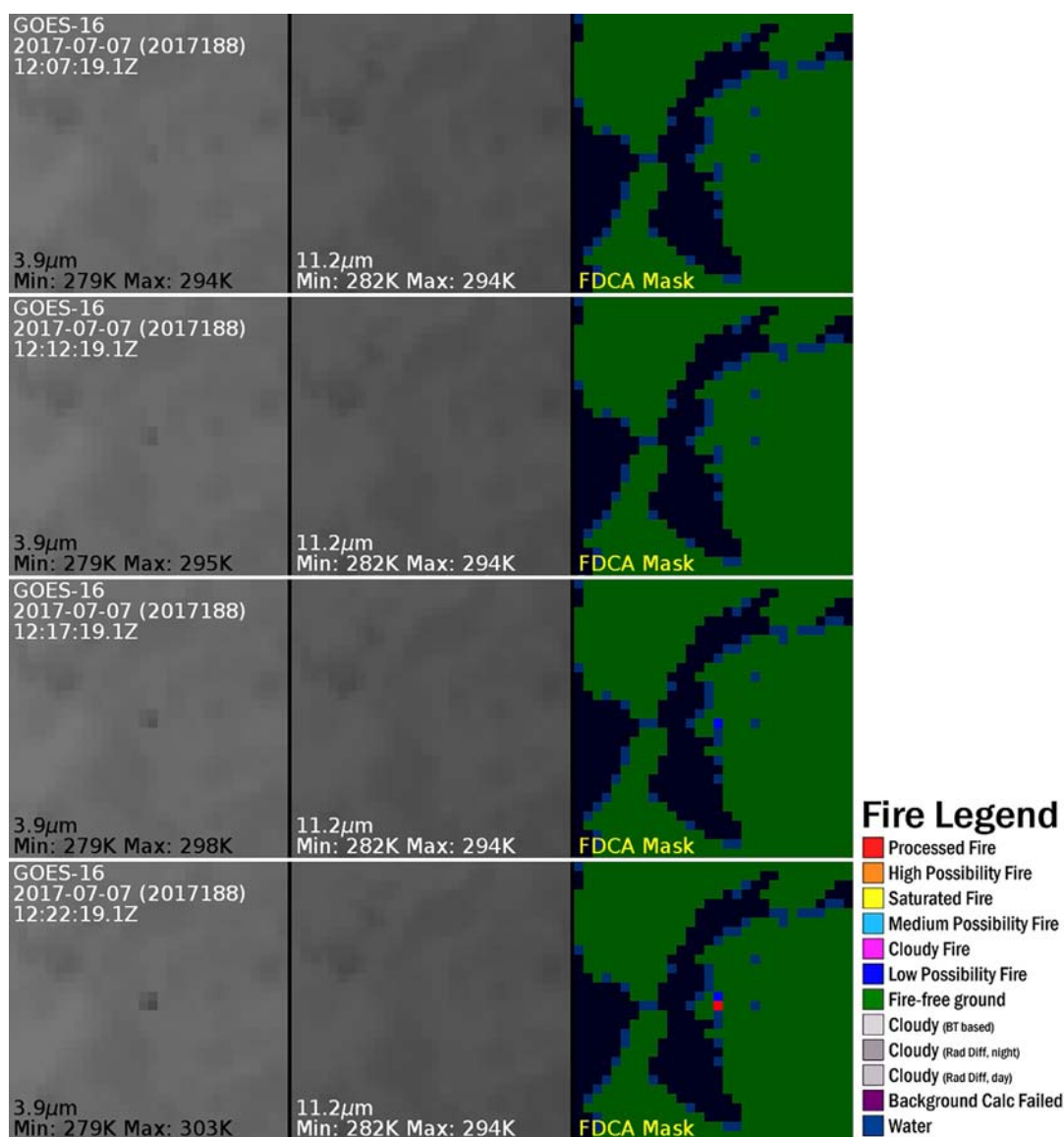


FIG. 13.5 Four time steps of the Oakland apartment building fire on July 7, 2017. As with earlier figures, darker is hotter in the 3.9- and 11.2- μ m images. Warming can be seen in the 3.9 μ m over the 20-min period. The metadata mask product from the FDCA is included in the right panel. FDCA first catches the fire 5 min after a human observer might, and in the final frame has classified the fire as “processed” and assigned the fire properties the Bay Area NWS Forecast Office observed. Animation 13.2 of this figure is available in the online version at <https://doi.org/10.1016/B978-0-12-814327-8.00013-5>.

to move southeast. Fig. 13.7 shows those fires at different times (Animation 13.4 in the online version at <https://doi.org/10.1016/B978-0-12-814327-8.00013-5>). The fire fronts moved so fast that some questioned whether the satellite was actually seeing the fire instead of the hot air from the upwind fire. Hot air lacks the bulk to produce such a strong signal, the signature seen in band 7 could only come from burning biomass. The high speed of the fire is attributed to “spotting”: flaming debris carried ahead of the fire line. It was this same spotting that foiled attempts to contain the blazes. Similar “spotting” has been observed with forest fires and other grassland fires (Hollandsworth, 2017).

A somewhat less extreme event, the Rhea fire of April 2018 in western Oklahoma, provides a good case to track fire properties of a large fire complex over time. Fig. 13.8 contains selected time steps of the fire during the first two days of the event, with associated temperature, size, and FRP fields and the metadata mask. These data were produced with a research version of the algorithm that provides FRP for all detected fire pixels. The total FRP for the fire complex shown in Fig. 13.8 is plotted in Fig. 13.9. ABI mesoscale scan data were used to generate the plot to show the



FIG. 13.6 Mesoscale sector 1 (MESO1) imagery covering the area around Drumright, Oklahoma, where NWS forecasters noted a small heat signature, approximately 1K above background that was found to be a house fire. The 3.9- μ m data are scaled two different ways, the left panel uses a typical default temperature scale while the right panel has been scaled to the data within the image. The house fire is hard to distinguish from the background when using the default scaling. Animation 13.3 of this figure is available in the online version at <https://doi.org/10.1016/B978-0-12-814327-8.00013-5>.

overall consistency despite minute-to-minute variations in the fire's behavior and intensity (Animation 13.5 in the online version at <https://doi.org/10.1016/B978-0-12-814327-8.00013-5>).

On the other side of the spectrum, Figs. 13.10 and 13.11 illustrate a controlled burn that occurred at the McHenry County Lock and Dam in Illinois on March 21, 2018. Residents of Crystal Lake who happened to attend high school with a member of the FDCA science team reported a large plume over the city, which was traced to a controlled burn of a marsh on Illinois state park land at the McHenry Lock and Dam on the Fox River. Numerous small controlled burns occurred on that day in the region. In this case, an image of the fire itself was obtained, very nearly coincident in time with one of the FDCA detections of the fire. The fire was not large at all, measuring under an acre at the time but showing a pretty good flame height. Fig. 13.10 shows the FDCA mask and band 7 imagery at various time steps (Animation 13.6 in the online version at <https://doi.org/10.1016/B978-0-12-814327-8.00013-5>). FDCA had a difficult time in this case due to low surface temperatures, which triggered its internal cloud screen and produced the large gray areas seen in the figure, areas that are clear as seen in the 0.64- μ m band imagery. Fig. 13.11 is the fire itself and the coincident satellite imagery from immediately before and after the photo was taken. The fire appears to occupy the usual 2 \times 2 pixel area, despite having a small flaming area and larger low-intensity smoldering component.

In the early hours of November 9, 2018, a fire began which would prove to be the most devastating to hit California up until that time. At about 6:30 AM PDT (14:30 UTC), a fire was reported near Paradise, California. It was not long before evacuations were ordered. Ultimately, the Camp Fire led to the destruction of the town of Paradise, dozens of deaths, and produced a choking pall of smoke that affected Sacramento and San Francisco and much of California for weeks.

Despite GOES-16's steep viewing angle and despite the terrain, ABI detected a radiance signal from the fire in its 6:22 AM PDT (14:22 UTC) scan. The signal was very weak, and most noticeable in the radiance difference field calculated by converting the 11.2- μ m brightness temperature to an equivalent 3.9- μ m radiance and taking the difference of that and the observed 3.9- μ m radiance, known as the radiance difference or radiance difference field. This radiance difference is a key component of FDCA, but it needs to reach a certain threshold (0.2 in this case) to be considered as a fire. Due to that requirement, the algorithm did not detect the fire until 6:52 AM PDT (14:52 UTC). When viewing the sequence of images in Fig. 13.13, the fire appears self-evident thanks to the temporal dimension. FDCA does not exploit that temporal dimension, forcing it to rely on thresholds that prevent false alarms due to other features. Those other features can be seen in Fig. 13.12, disappearing as the scale adjusts for the intensity of the Camp Fire (Animation 13.7 in the online version at <https://doi.org/10.1016/B978-0-12-814327-8.00013-5>). However, the fact that we can identify the fire by eye is a strong argument for developing a fire detection algorithm that takes full advantage of the temporal dimension provided by ABI-class sensors.

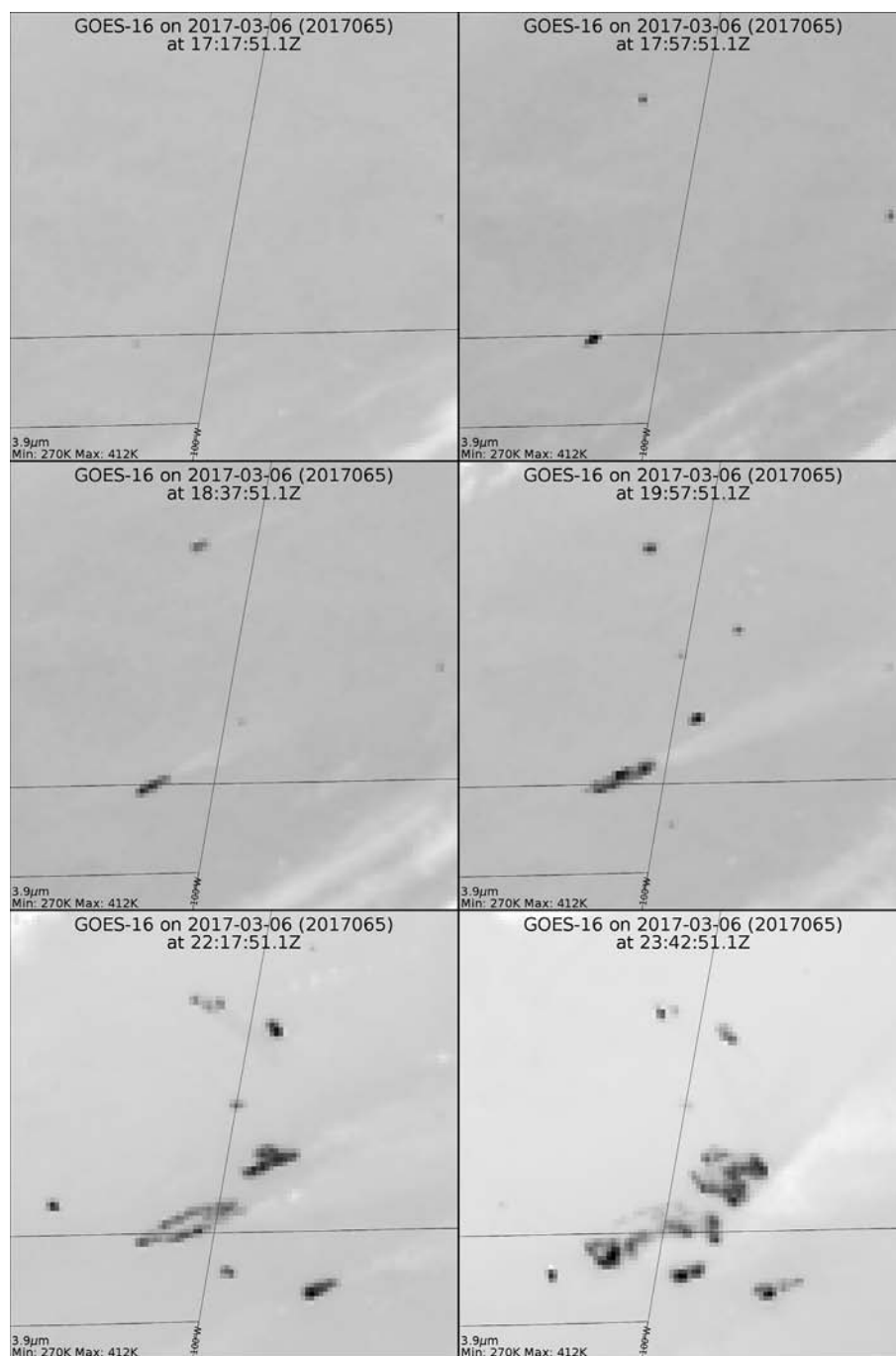


FIG. 13.7 Dynamically scaled 3.9- μm data over portions of Oklahoma and Kansas showing rapid evolution of grass fires that were stoked by high winds. As a front came through later in the day, the fires made an almost 90° turn to the southeast. Animation 13.4 of this figure is available in the online version at <https://doi.org/10.1016/B978-0-12-814327-8.00013-5>.

13.5 VALIDATING SATELLITE FIRE PRODUCTS

Satellites have a unique perspective on fires, one not matched by any record keeping on the ground. Large events in the United States tend to be well documented and may be found on InciWeb (<http://inciweb.nwcg.gov>), an interagency resource for fire information. Some counties and parishes in the United States regulate controlled burns and they have records of varying quality, often specifying times to within a day or week. In some states, they record the fire location as the site of the county seat or the centroid of the county, making the data useless for validation.

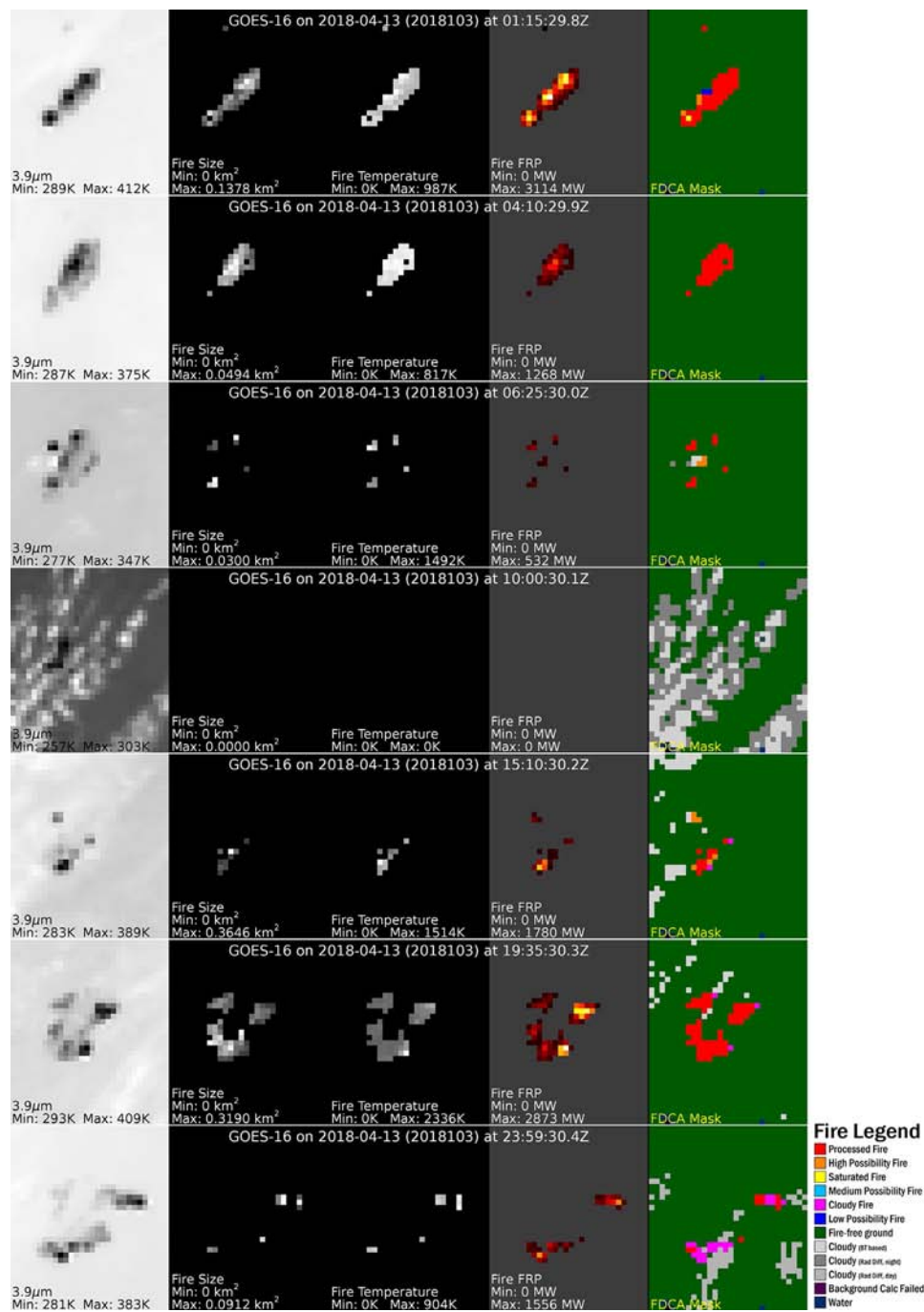


FIG. 13.8 Seven selected times from the Rhea Fire on April 13, 2018 showing the dynamically scaled 3.9- μ m data, and the four FDCA output fields. FRP is shown in color from black to red for 0–1000 MW, red to yellow for 1000–2000 MW, and yellow to white for 2000–3000 MW. Animation 13.5 of this figure is available in the online version at <https://doi.org/10.1016/B978-0-12-814327-8.00013-5>.

The vast majority of satellite-detected fires are undocumented in any meaningful way. Therefore, as paradoxical as it may seem, validation of satellite detected and characterized fires is best accomplished using satellite data.

For GOES-16, a three-tier approach for validation was developed: visual inspection, comparison to moderate resolution polar-orbiting satellite fire detection data, comparison to WFABBA data from GOES-13 and -15, and comparison to very high resolution data from low Earth orbit satellite instruments like Landsat Operational Land Imager (OLI) and the Advanced Spaceborne Thermal Emission and Reflection Radiometer (ASTER), which have pixel footprints in the 30–90-m range. While case study comparison is possible with data obtained from instruments on planes or drones, very little of that data is available.

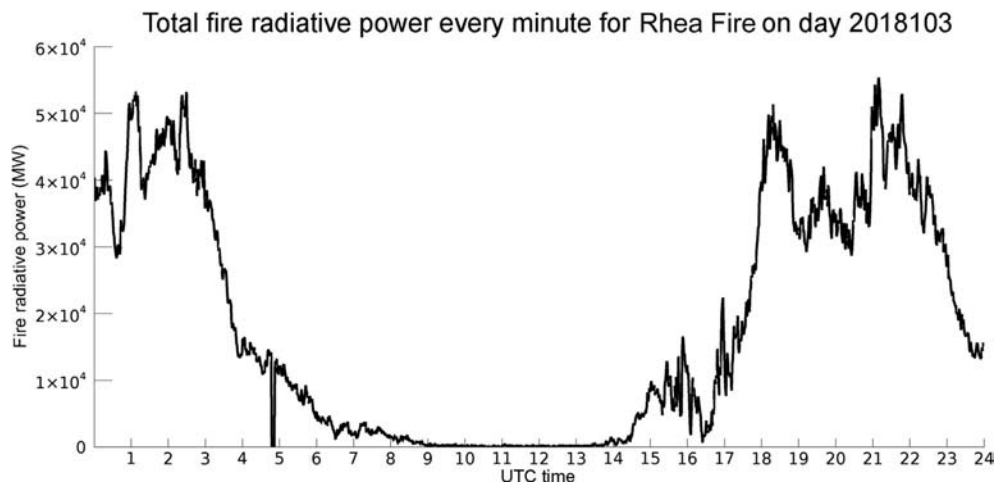


FIG. 13.9 Total FRP for the Rhea Fire complex on April 13, 2018, calculated from FDCA FRP generated from the 1-min MESO1 sector ABI 3.9- μm data. The overall pattern is diurnal, as is typically seen with large fires that intensify during the warmer parts of the day when winds tend to pick up. Variations are introduced by changes in the fire driven by the weather, particularly wind speed and direction changes and intervening cloud cover.

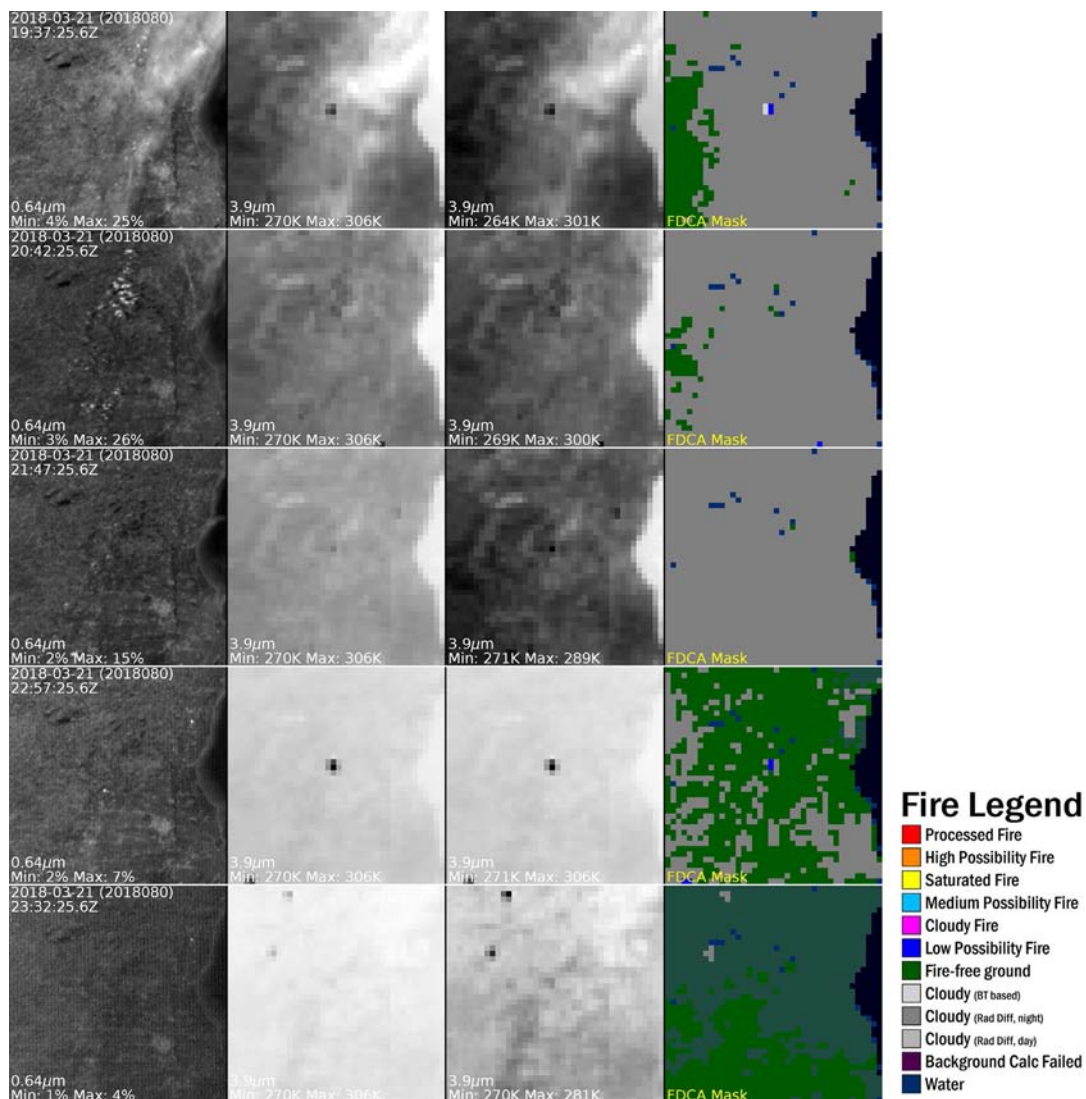


FIG. 13.10 ABI data from select times centered on a prescribed burn of a marsh at the McHenry County Lock and Dam in Illinois on March 21, 2018. While the 0.64 μm is dynamically scaled, the 3.9 μm is presented with both a fixed scaling (270–306K) and dynamic scaling to show how the overall scene changed that afternoon. The FDCA metadata mask shows that the algorithm had a difficult time identifying that fire, which was due to the relatively cold surface temperatures (often <270 K in the 3.9- and 11.2- μm bands). Animation 13.6 of this figure is available in the online version at <https://doi.org/10.1016/B978-0-12-814327-8.00013-5>.



FIG. 13.11 Photo of the McHenry County Lock and Dam prescribed burn from the ground level. The actively flaming area was relatively small, no more than about an acre and possibly less. The smoldering area was larger, but was relatively cool and not a major contributor to the satellite detected radiance in the 3.9- μm band. ABI data (as seen in Fig. 13.10) immediately prior to and following the time the photograph was taken is shown.

Visual inspection, examination of 3.9- μm data, perhaps in conjunction with the visible bands, 11.2- μm band, and the radiance difference field, is a simple and effective, yet time consuming, way of assessing whether a detected fire was a commission error, and to get an idea of what the algorithm may be omitting. In addition, the patterns of fires are somewhat predictable, and visually examining an image of the metadata mask is a good way to quickly identify problems. Fig. 13.13 shows one example of the mask from a development version of the code alongside band 7 and the radiance difference field for a scan over CONUS. Suspicious areas in the mask are highlighted. Monitoring the mask in this fashion is a useful way to perform routine validation—it does not guarantee that all issues will be caught, but major problems are easy to identify.

ABI fire detection and characterization comparisons with polar-orbiting imagers such as the Visible Infrared Imaging Radiometer Suite (VIIRS) and Moderate Resolution Imaging Spectroradiometer (MODIS), and with other GOES provides a large number of matchups to work with, though not without caveats. The polar platforms can detect smaller fires than ABI, so we know there will be omissions. In cases where fires do match in time and space, the viewing geometry and terrain can provide one platform with a much better view than another. Fig. 13.14 illustrates such a case, from March 14, 2018 showing GOES-15 (17:45 UTC) and GOES-16 (17:47 UTC) side by side at almost exactly the same time,

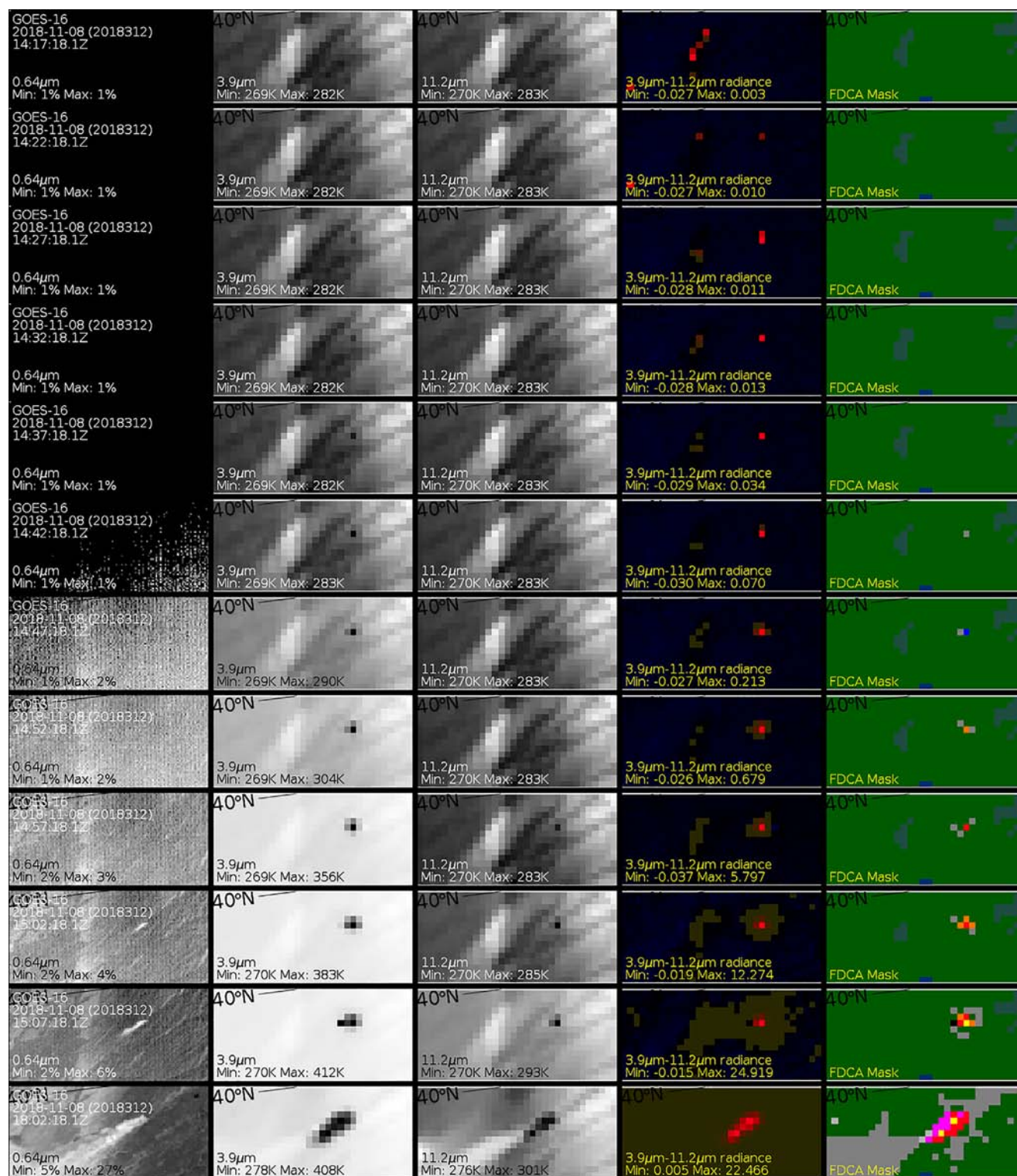


FIG. 13.12 Dynamically scaled ABI and FDCA data from the beginning of the Camp Fire. The leftmost panel of each row is 0.64- μm data, which is dominated by noise until the Sun rises. Dynamically scaled 3.9- and 11.2- μm data is shown in the next two panels. The fourth panel includes the radiance difference between the 3.9- and 11.2- μm bands represented in 3.9- μm radiance space. That radiance difference shows the Camp Fire at 14:22 UTC, prior to it being clearly discernible in the 3.9- μm data. The difference was initially very small, however, and it wasn't clearly a fire until later. The FDCA metadata mask is in the rightmost panel and was produced using a research version of the algorithm. Animation 13.7 of this figure is available in the online version at <https://doi.org/10.1016/B978-0-12-814327-8.00013-5>.

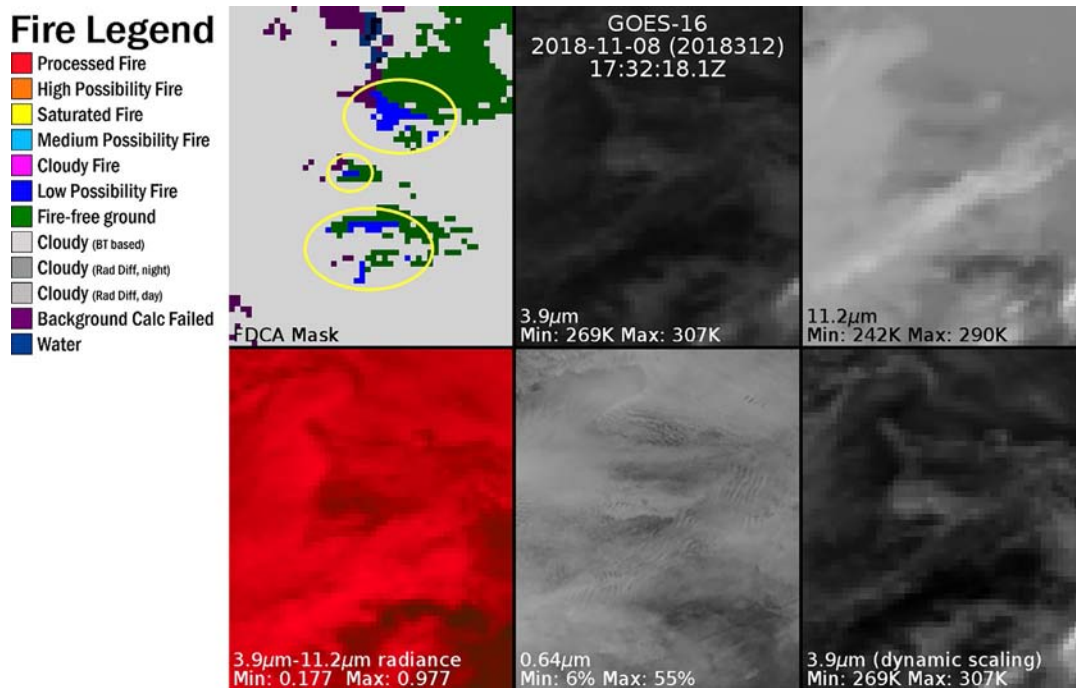


FIG. 13.13 A suspect area of the fire algorithm results over the Carolinas on November 8, 2018, the day of the Camp Fire. The upper row includes the FDCA metadata mask and the 3.9- and 11.2- μm data scaled from 240 to 310 K, which highlights how much warmer the entire 3.9- μm scene is at this time during the day. The lower row includes the 3.9 minus 11.2- μm radiance difference in 3.9- μm space (which is fairly large throughout the scene), 0.64- μm data using the default grayscale for visible data and showing mostly cloudy conditions, and then 3.9- μm data dynamically scaled to the scene to improve contrast. The highlighted suspect areas of low possibility fire pixels occur in places where the 3.9- μm looks relatively warm. The clouds in the scene are a complex mixture of water and ice clouds, and water clouds reflect 3.9- μm radiation, which causes the entire scene to appear warm compared to the 11.2- μm , and particularly so in some places, and in those places the algorithm finds low possibility fires and sometimes fails to make a background determination.

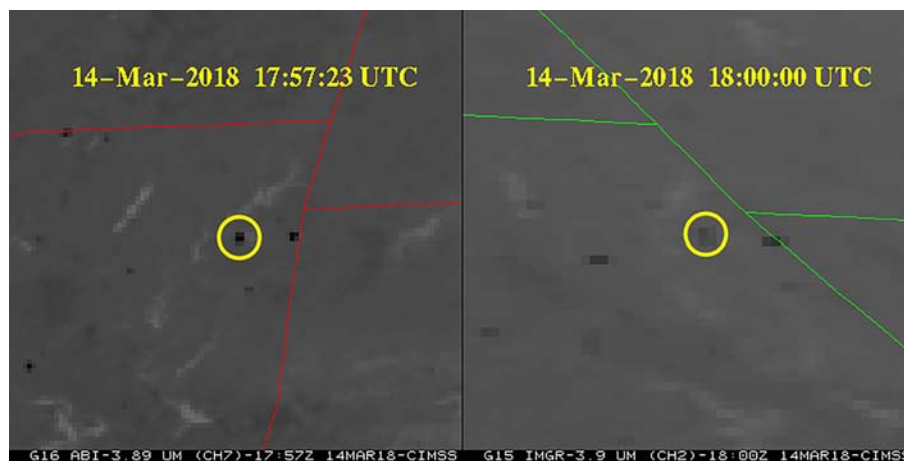


FIG. 13.14 Comparison of GOES-15 (right) and GOES-16 (left) 3.9- μm data over eastern Oklahoma, southwestern Missouri, and western Arkansas on March 14, 2018. The highlighted fire is located on a mountainside that primarily faces east, making it hard to see from the GOES-15 position at approximately 135°W. GOES-16 was located at 75.2°W. In other cases, fires look similar, and in still others, fire differs in appearance, mostly due to terrain effects as in the highlighted case.

with a view over eastern Oklahoma. The highlighted fire shows up more clearly in GOES-16 ABI data than GOES-15 imager data, even accounting for the resolution differences. Notably, other fires in the scene are comparably hot. FRP is the common characterization product for all platforms, and it can be validated through matchups as well.

Whether considering detection or FRP validation, the viewing geometry for each satellite needs to be accounted for, and diffraction can also cause a substantial difference in detected energy on a case-by-case basis, not to mention the remapping that occurs for both ABI and VIIRS data. Trends over time and comparison with a large number of

matchups are the best way to assess how well the satellites are characterizing FRP. In addition, feedback from the modeling community is also helpful—if the FRP trends are wrong, they'll see it in the comparison of their model's smoke output to satellite imagery. For those users the trends take priority over the absolute accuracy of the FRP data. Adding a scaling factor and/or bias for satellite FRP data is less bothersome than random error.

Very high-resolution data from platforms such as Landsat-8 or ASTER on Terra provide a very useful way to assess detection accuracy. They provide a detailed view of the fire and separating fire pixels from non-fire pixels is relatively easy thanks to that high spatial resolution. Unfortunately, the number of available scenes is limited, but over the course of months, hundreds of matchups are possible. While labor intensive, these matchups are the best for determining omission and commission error rates, as well as identifying factors that may be leading to either type of error.

13.6 SUMMARY AND LOOKING AHEAD

Not long before the launch of ABI, wildfire monitoring was primarily associated with forest fires, events often in the domain of the USFS. They were the most frequent events and grabbed the largest share of the public's attention. The utility of fire detection extends well beyond forest fires that are often managed to minimize damage to life and property but rarely directly affect large population centers. ABI's fire monitoring capabilities have yet to be fully utilized; the value of the temporal dimension is tremendous but utilizing it requires rethinking the algorithm and even processing architecture in order to achieve the low latency that early fire detection requires. Short of such a radical redesign, the existing algorithm can make better use of ABI data by employing the 0.86-, 1.6-, 2.2-, and/or 10.3- μm bands to improve the cloud screening and background characterization. Users such as NWS incident meteorologists (IMETs) have expressed a need for information about fire events rather than single pixel information, to help them track the progress of a fire complex and also to help the separate the smaller fires that appear briefly from the longer-term events that they are concerned with. Such a product would be produced from aggregating FDCA output and releasing updates at a rate those users deem suitable.

The physical basis, requirements specification, and planned validation of individual geophysical algorithms are described in the Algorithm Theoretical Basis Documents for each product and may supplement the material in the individual chapters. These documents can be found at the NOAA Center for Satellite Applications and Research website at https://www.star.nesdis.noaa.gov/goesr/documentation_ATBDs.php. Additional documents and other user resources are found at the GOES-R Series website <https://www.goes-r.gov/>. ABI data are archived at NOAA's Comprehensive Large Array-data Stewardship System (CLASS): <https://www.class.noaa.gov/>. The ABI imagery shown in this manuscript from before December 18, 2017 is considered preliminary and nonoperational. Additional GOES-R/16 references can be found at <https://www.goes-r.gov/resources/Scipubs/index.html> while more imagery and other ABI information can be found at: <https://cimss.ssec.wisc.edu/goes/goesdata.html>.

Acknowledgments

The author would like to thank Elaine Prins and Paul Menzel for starting the geostationary fire detection program; Joleen Feltz, Jason Brunner, and Jay Hoffman for their work on the WFABBA; Jeffrey Reid, Edward Hyer, and Shobha Kondragunta for their support of geostationary fire products over the years; Ivan Csiszar, Wilfrid Schroeder, and Joanne Hall for their past and ongoing work validating the WFABBA and FDCA. This work was supported by National Oceanic and Atmospheric Administration CIMSS CA grant #NA15NES4320001. The views, opinions, and findings contained in this report are those of the authors and should not be construed as an official National Oceanic and Atmospheric Administration or US Government position, policy, or decision.

References

- Hollandsworth, Skip, 2017. The Day the Fire Came. Texas Monthly. July 2017. <<https://features.texasmonthly.com/editorial/the-day-the-fire-came/>> (Accessed 19.12.2018).
- Lindley, T.T., Anderson, A.R., Mahale, V.N., Curl, T.S., Line, W.E., Lindstrom, S.S., Bachmeier, A.S., 2016. Wildfire detection notifications for impact-based decision support services in Oklahoma using geostationary super rapid scan satellite imagery. *J. Oper. Meteor.* 4 (14), 182–191.
- Matson, M., Dozier, J., 1981. Identification of subresolution high temperature sources using a thermal IR sensor. *Photogramm. Eng. Remote. Sens.* 47, 1311–1318.
- McNamara, D., Stephens, G., Ramsay, B., Prins, E., Csiszar, I., Elvidge, C., Hobson, R., Schmidt, C., 2002. Fire detection and monitoring products at the National Oceanic and Atmospheric Administration. *Photogramm. Eng. Remote. Sens.* 68, 774–775.

- Prins, E., Menzel, W.P., 1992. Geostationary satellite detection of biomass burning in South America. *Int. J. Remote Sens.* 13 (15), 2783–2799.
- Prins, E.M., Menzel, W.P., 1994. Trends in south American biomass burning detected with the GOES visible infrared spin scan radiometer atmospheric sounder from 1983 to 1991. *J. Geophys. Res.-Atmos.* 99, 16,719–16,736.
- Prins, E., Schmidt, C., 2001. GOES burns bright. *Geospat. Sol.* 11 (7), 33.
- Wooster, M.J., Zhukov, B., Oertel, D., 2003. Fire radiative energy for quantitative study of biomass burning: Derivation from the BIRD experimental satellite and comparison to MODIS fire products. *Remote Sens. Environ.* 86, 83–107.

Further Reading

- Al-Saadi, J., Szykman, J., Pierce, R.B., Kittaka, C., Neil, D., Chu, D.A., Remer, L., Gumley, L., Prins, E., Weinstock, L., MacDonald, C., Wayland, R., Dimmick, F., Fishman, J., 2005. Improving national air quality forecasts with satellite aerosol observations. *Bull. Am. Meteorol. Soc.* 86 (9), 1249–1261.
- Dozier, J., 1981. A method for satellite identification of surface temperature fields of subpixel resolution. *Remote Sens. Environ.* 11, 221–229.
- Freitas, S.R., Longo, K.M., Silvas Dias, M.A.F., Silva Dias, P.L., Chatfield, R., Prins, E., Artaxo, P., Grell, G.A., Recuero, F.S., 2005. Monitoring the transport of biomass burning emissions in South America. *Environ. Fluid Mech.* 5 (1), 135–167.
- Giglio, L., Descloitres, J., Justice, C.O., Kaufman, Y., 2003. An enhanced contextual fire detection algorithm for MODIS. *Remote Sens. Environ.* 87, 273–282.
- Hyer, E.J., Reid, J.S., Prins, E.M., Hoffman, J.P., Schmidt, C.C., Meittinen, J.L., Giglio, L., 2013. Patterns of fire activity over Indonesia and Malaysia from polar and geostationary satellite observations. *Atmos. Res.* 122, 504–519.
- Justice, C.O., Giglio, L., Korontzi, S., Owens, J., Morisette, J., Roy, D., Descloitres, J., Alleaume, S., Petitcolin, F., Kaufman, Y.J., 2002. The MODIS fire products. *Remote Sens. Environ.* 83, 244–262.
- Koltunov, A., Ustin, S.L., Prins, E.M., 2012. On timeliness and accuracy of wildfire detection by the GOES WF-ABBA algorithm over California during the 2006 fire season. *Remote Sens. Environ.* 127, 194–209.
- Reid, J.S., Prins, E.M., Westphal, D.L., Schmidt, C.C., Richardson, K.A., Christopher, S.A., Eck, T.F., Reid, E.A., Curtis, C.A., Hoffman, J.P., 2004. Real-time monitoring of south American smoke particle emissions and transport using a coupled remote sensing/box-model approach. *Geophys. Res. Lett.* 31 (6).
- Reid, J.S., Hyer, E.J., Prins, E.M., Westphal, D.L., Zhang, J., Wang, J., Christopher, S.A., Curtis, C.A., Schmidt, C.C., Eleuterio, D.P., Richardson, K.A., Hoffman, J.P., 2009. Global monitoring and forecasting of biomass-burning smoke: Description of and lessons from the fire locating and modeling of burning emissions (FLAMBE) program. *IEEE J. Sel. Top. Appl. Earth Observ. Remote Sens.* 2 (3), 144–162.
- Schmit, T.J., Lindstrom, S.S., Gerth, J.J., Gunshor, M.M., 2018. Applications of the 16 spectral bands on the Advanced Baseline Imager (ABI). *J. Oper. Meteor.* 6 (4), 33–46. <https://doi.org/10.15191/nwajom.2018.0604>.
- Schroeder, W., Prins, E., Giglio, L., Csiszar, I., Schmidt, C., Morisette, J., Morton, D., 2008a. Validation of GOES and MODIS active fire detection products using ASTER and ETM+ data. *Remote Sens. Environ.* 112 (5), 2711–2726.
- Schroeder, W., Ruminiski, M., Csiszar, I., Giglio, L., Prins, E., Schmidt, C., Morisette, J., 2008b. Validation analyses of an operational fire monitoring product: The Hazard mapping system. *Int. J. Remote Sens.* 29 (20), 6059–6066.
- Schroeder, W., Csiszar, I., Giglio, L., Schmidt, C.C., 2010. On the use of fire radiative power, area, and temperature estimates to characterize biomass burning via moderate to coarse spatial resolution remote sensing data in the Brazilian Amazon. *J. Geophys. Res. Atmos.* 115 (21), 1–10.
- Weaver, J.F., Lindsey, D., Bikos, D., Schmidt, C.C., Prins, E., 2004. Fire detection using GOES rapid scan imagery. *Weather Forecast.* 19 (3), 496–510.
- Zhang, X., Kondragunta, S., Schmidt, C., Kogan, F., 2008. Near real time monitoring of biomass burning particulate emissions (PM_{2.5}) across contiguous United States using multiple satellite instruments. *Atmos. Environ.* 42, 6959–6972.
- Zhang, X., Kondragunta, S., Ram, J., Schmidt, C., Hung, H., 2012. Near-real-time global biomass burning emissions product from geostationary satellite constellation. *J. Geophys. Res.-Atmos.* 117 (14), 1–18.